SCIENCE CHINA
Physics, Mechanics & Astronomy

• Invited Review •

February 2015 Vol. 58 No. 2: 027001
doi: 10.1007/s11433-014-5627-6

Laser beam induced current microscopy and photocurrent mapping for junction characterization of infrared photodetectors

QIU WeiCheng & HU WeiDa*

National Laboratory for Infrared Physics, Shanghai Institute of Technical Physics, Chinese Academy of Sciences, Shanghai 200083, China

Received September 1, 2014; accepted November 5, 2014; published online December 17, 2014

For non-destructive optical characterization, laser beam induced current (LBIC) microscopy has been developed into as a quantitative tool to examine individual photodiodes within a large pixel array. Two-dimensional LBIC microscopy, also generally called photocurrent mapping (PC mapping), can provide spatially resolved information about local electrical properties and p-n junction formation in photovoltaic infrared (including visible light) photodetectors from which it is possible to extract material and device parameters such as junction area, junction depth, diffusion length, leakage current position and minority carrier diffusion length etc. This paper presents a comprehensive review of research background, operating principle, fundamental issues, and applications of LBIC or PC mapping.

laser beam induced current, photocurrent mapping, focal plane array, photocurrent, infrared photodetector

PACS number(s): 52.70.Kz, 61.80.Ba, 85.30.De

Citation: Qiu W C, Hu W D. Laser beam induced current microscopy and photocurrent mapping for junction characterization of infrared photodetectors. Sci China-Phys Mech Astron, 2015, 58: 027001, doi: 10.1007/s11433-014-5627-6

1 Introduction

Semiconductor-based focal plane arrays (FPAs) are arranged into large two-dimensional arrays for use in staring imaging systems. Individual detectors in the array represent a pixel in the resulting image. Therefore, any nonuniformity in the array can result in a serious impact on the performance of the FPA, and limit the yield of devices in large infrared arrays, resulting in low yields and high unit cost. Laser beam induced current (LBIC) microscopy has proven useful for quick and non-destructive measurement for the junction performance of each pixel in large arrays at an early stage in the fabrication process. Therefore, significant cost savings and processing improvement would be expected in FPAs. The LBIC spectrum was first investigated by Wallmark [1] in 1957, who successfully explained the lateral photo-effect behind the LBIC phenomena. Through measuring the current signal rather than the voltage signal, the LBIC method was first used as a non-destructive tool in HgCdTe material from the work in the mid 1980's by Bajaj et al. [2]. In 2000, LBIC as a potential characterization tool for quantitative extraction of zero-bias resistance-area product (R_0A) in photodiodes was reported by Musca et al. [3] LBIC measurements indicated that the peak LBIC signal for the hydrogenated long wavelength diode (R_0A=70 Ω cm^2) is approximately a factor of two greater than the non-hydrogenated long wavelength diode (R_0A=8 Ω cm^2). A detailed interpretation of the physical mechanisms involved in the generation of laser beam induced current in p-n junction diodes was then reported by Redfern et al. [4]. It was found that the net current signal is a combination of carrier drift in the built-in electric field and diffusion due to the concentration gradient. LBIC imaging reflects the spatially resolved information about electrical characteristics and localized nonuniformities. Specifically, HgCdTe-based photovoltaic

---

*Corresponding author (email: wdhu@mail.sitp.ac.cn) infrared detectors easily suffer from temperature and photo active defects due to their narrow band gap and complex manufacturing processes. The effects of junction type conversion dependence on temperature, ion implantation induced defects and mixed conduction in long-wavelength HgCdTe p-n junction were obtained based on the junction transformation model for LBIC measurements under different temperatures [5,6]. The non-ideal effect of localized leakage in p-n junctions can also be investigated by the LBIC method [7–10]. It is indicated that when the leakage point is asymmetric inside the device, the asymmetry in the LBIC line profile can be obtained by considering the leakage as a small junction region with extremely short carrier lifetime along the horizontal portion of the junction. Feng et al. [7] reported the dominant leakage current mechanisms in vacancy-doped $Hg_{1-x}Cd_xTe$ (x=0.31) photodiodes by measuring LBIC signals at different temperatures. The key parameters of photoelectric diodes such as carrier diffusion length and junction depth were extracted from LBIC measurements and reported in refs. [11–13]. Vacancy-doped p-type HgCdTe is possibly converted into n-type by various etching processes, such as most commonly used ion implantation [14,15] or pulse laser drilling [16–18], nano printing [19], or reactive ion etching [20]. Those etching-induced junctions can all be characterized by LBIC profiles.

However, analysis of LBIC profiles of photovoltaic detectors has been acknowledged as a difficult task because of the large number of factors influencing LBIC signals; typically for narrow band-gap infrared photodetectors [21,22]. These factors include geometrical parameters of the specific device structure including contact locations and device length, width, depth, and material properties including the bandgap, doping profile, carrier lifetime, and diffusion length. Additionally, other non-ideal effects such as localized junction leakage and surface recombination, and non-Ohmic contacts contribute to difficulty in analysis. In the past, most of the LBIC research used for nondestructive characterization of photodiodes has been half-qualitative or empirical [23,24]. Further research shows that quantitative extraction of these parameters from LBIC profiles is very important for making the technique more efficient in semiconductor characterization [5,6,8,25]. Numerical simulation using the standard drift-diffusion model for LBIC [26–30] is commonly used for quantitative study of the LBIC phenomenon. Lately, two-dimensional scanning photocurrent (PC) mapping has been widely used in emerging nanodevices with two-dimensional materials [31–33]. It has been an efficient characterization method for nano-scale photovoltaic visible/infrared photodetectors [34–36].

This review is an attempt to systematically categorize and summarize the research activities dealing with principles, models and applications of LBIC and PC mapping. It is expected to provide a reliable reference for LBIC and PC mapping characterizations of third-generation focal plane array infrared photodetectors (small pixels), photovoltaic devices based on artificial microstructures, and heterojunction photovoltaic nano-devices with two-dimensional materials.

2 Device description and LBIC setup

High performance infrared focal plane arrays (IRFPAs) incorporate a large number of pixels. Each pixel commonly consists of two parts—a photodetector element and a Si readout integrated circuit (ROIC) element which includes signal processing such as gain control, offset control and readout. IRFPAs are assembled by indium bonding corresponding elements of a photodetector array and silicon readout circuit as shown in Figure 1.

In preparation for the experiment, only two shorted Ohmic contacts would be constructed at remote positions on either side of the device(s). The principle of p-n junction array LBIC testing is schematically represented in Figure 2. He-Ne laser irradiance at a wavelength of 632.8 nm is focused onto the surface of the semiconductor, and stepped incrementally across the sample in the horizontal direction. When the laser spot is more than a few carriers diffusion lengths from a built-in electric field, the photogenerated electron-hole pairs recombine without reaching junction

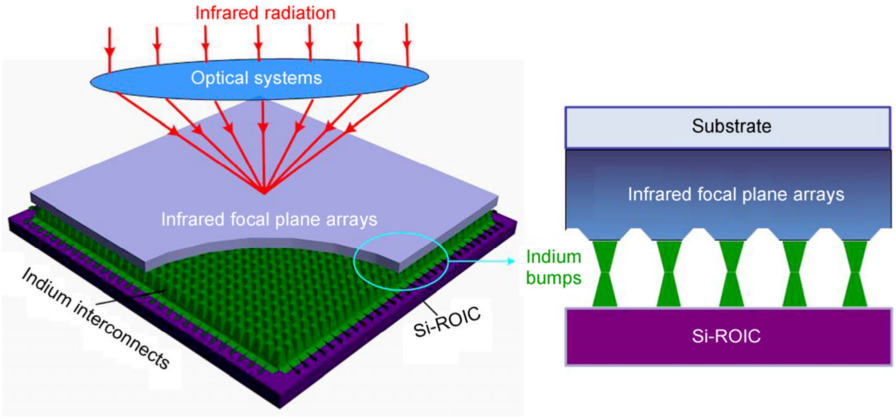

Figure 1 (Color online) Schematic diagram of focal plane array photovoltaic infrared detector.

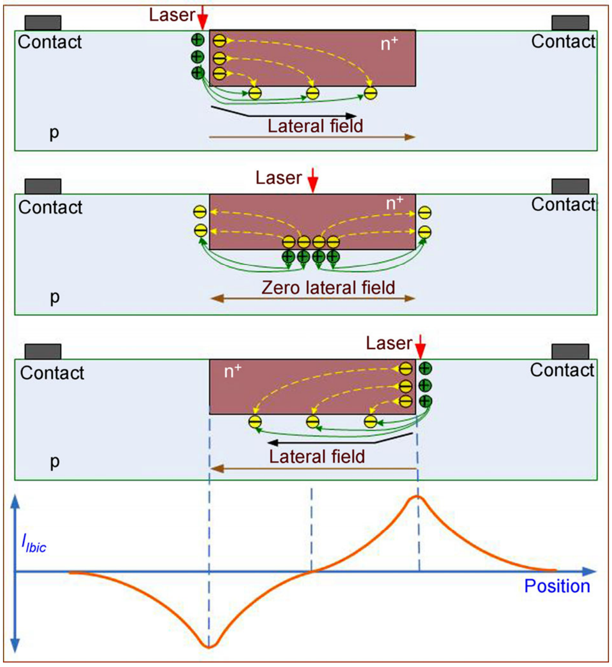

Figure 2 (Color online) The principle of a single n^+-on-p pixel LBIC testing. Reprinted with permission from ref. [26] © 2014, American Institute of Physics.

region and no current signal can be induced. In contrast, if the photogenerated electron-hole pairs can diffuse and be separated by the built-in electric field, the separated carriers seek to recombine via returning current paths, which could be both the internal and external closed circuits; incidentally an induced current can be measured.

The LBIC profile presents the positive and negative bimodal distribution according to the three typical positions of a laser spot on the surface of the sample. This is explained by assuming the direction from right to left of device as the direction of negative current flow.

Case 1: Illumination on the left of p-type region close to the junction. If the laser is focused onto the surface of the p-type region close to the junction, the photogenerated carriers that are separated by the built-in electric field would provide excess electrons (denoted by "–") into the n-type region while excess holes (denoted by "+") remain in the p-type region. Since the conductivity of the n-type region is nearly two orders of magnitude more than that in the p-type region, the excess electrons can quickly redistribute themselves over the region uniformly. A reinjection of electrons can occur in the underlying p-type region. Finally, the presence of these excess holes and electrons constitutes a localized forward bias of the junction (direction from left to right), that drives the excess carriers to seek any possible returning current paths for recombination. Among these paths, the returning current via the external circuit contribute to the LBIC's negative signal.

Case 2: Illumination on the right of p-type region close to the junction. This situation is similar to the previous analysis, the photogenerated carriers diffuse and are separated by the built-in electric field, resulting in excess electrons passing into the n-type region while excess holes pass into the p-type region. However, a localized forward bias of the junction in the opposite direction (from right to left) is formed. Therefore, a positive LBIC signal can be obtained.

Case 3: Illumination on the surface of n-type region. A unique feature in the situation where the laser is focused onto the surface of the n-type region was the appearance of two types of returning current flows in the opposite direction. If the laser spot is exactly located in the middle of n-type region, two opposite return current flows will cancel each other, producing a zero net LBIC signal.

Two different structures of the laser beam induced current (LBIC) test system are shown in Figure 3. The test system typically consists of a laser light source, CCD camera, computer, temperature controller, and an induced current measuring system with a lock-in amplifier. The sample is placed in a Dewar of liquid nitrogen controlled by the temperature controller. The He-Ne laser is focused to a spot of 1–1.5 μm in diameter which is stepped across the sample. The induced current is recorded by a SR830 DSP lock-in amplifier as a function of *x*-*y* scanning coordinates to provide a spatial LBIC map. The main difference between the two LBIC test systems is the method used to scan the samples. In Figure 3(a), the sample is scanned on a two-dimensional mobile platform driven by the computer. Another method is the use of a two-dimensional scanning galvo system to precisely control the direction of the laser beam by the computer, as shown in Figure 3(b).

3 Modeling and simulation of LBIC

In this section, analysis models are presented to quantitative study of the LBIC phenomenon. The standard two-dimensional steady-state drift-diffusion model for LBIC was first considered in ref. [27]. For the plain drift-diffusion simulation the well-known Poisson equation and continuity equations are used [28–30,37].

The steady-state continuity equations for electrons and holes are

$$\nabla\cdot\boldsymbol{J}_n = q(R-G)+q\frac{\partial n}{\partial \tau}, \tag{1}$$

$$\nabla\cdot\boldsymbol{J}_p = q(R-G)-q\frac{\partial p}{\partial \tau}. \tag{2}$$

Poisson's equation is

$$\nabla\varepsilon\cdot\nabla\psi = -q\left(p-n+N_{D^+}-N_{A^-}\right). \tag{3}$$

Here, *G* is the carrier generation rate, and *R* is the carrier recombination rate. The electron and hole current densities are listed as follows:

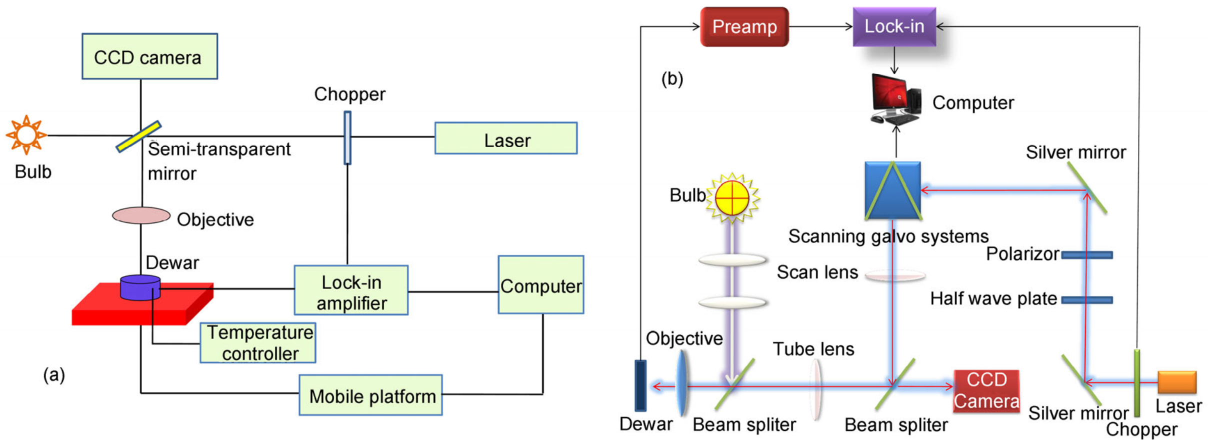

Figure 3 (Color online) Two different structure frames of laser beam induced current (LBIC) test system. (a) Scanning is performed by changing position of sample under control of a two-dimensional mobile platform; (b) scanning is performed by changing the direction of the laser beam under control of a scanning galvo system.

$$\boldsymbol{J}_n = qnu_n\boldsymbol{E}_n + qD_n\nabla n, \tag{4}$$

$$\boldsymbol{J}_p = qpu_pE_p - qD_p\nabla p, \tag{5}$$

where J_n and J_p are the electron and hole current densities respectively. n and p are the concentrations of the electrons and holes, respectively. ε is the permittivity of the semiconductors, q is the electron charge, and ψ is the electrostatic potential. E_n and E_p are the electron and hole effective electric fields, D_n and D_p are the electron and hole diffusion coefficients, and μ_n and μ_p represent the electron and hole mobility respectively.

The photo-generation is simulated by raytracing [38]:

$$G^{\text{opt}}(z,t) = J(x,y,z_0)\alpha(\lambda,z)\exp\left(-\left|\int_{z_0}^{z}\alpha(\lambda,z)\mathrm{d}z\right|\right), \tag{6}$$

where $\alpha(\lambda, z)$ is the absorption coefficient of HgCdTe material, λ is the wavelength, $J(x, y, z_0)$ is the optical intensity, and z_0 is the position along the ray where absorption begins.

The carrier generation-recombination process consists of Auger, radiative, and Shockley-Read-Hall (SRH) recombination terms, the detail descriptions of the models are as follows [39–42]:

$$R_{\text{RSH}} = \frac{pn - n_i^2}{\tau_p\left[n + n_i\exp\left(\frac{E_t - E_i}{kT}\right)\right] + \tau_n\left[p + n_i\exp\left(\frac{E_i - E_t}{kT}\right)\right]}, \tag{7}$$

$$R_{\text{Auger}} = (\gamma_n n + \gamma_p p)(pn - n_i^2), \tag{8}$$

$$R_{\text{Rad}} = C_{\text{Rad}}(pn - n_i^2), \tag{9}$$

where n_i and E_i are the intrinsic carrier concentration and intrinsic Fermi level respectively. E_{t} is the recombination center level. γ_n and γ_p are the Auger recombination coefficients respectively, and C_{Rad} is the radiative recombination coefficient for infrared detectors. Auger and radiative recombinations occur in narrow bandgap photovoltaic detectors. Auger recombination increases with temperature and becomes dominant near room temperature [6]. SRH recombination can be reduced by improving the fabrication procedure.

In order to account for the tunneling effects of the infrared devices, trap-assisted tunneling (TAT) and band-to-band tunneling (BBT) are added in the generation-recombination processes [43]. The generation rate G_{bbt} of BBT tunneling is described as:

$$\mathrm{G}_{\text{bbt}} = A_{\text{bbt}}\cdot E^2\cdot\exp\left(-\frac{B_{\text{bbt}}}{E}\right). \tag{10}$$

Here, A_{bbt} and B_{bbt} are the two different characterization parameters, and E is the electric field. The generation rate R_{tat} in trap-assisted tunneling process is given by [43]

$$R_{\text{tat}} = \frac{pn - n_i^2}{\frac{\tau_p}{1+\Gamma_p}\left[n + n_i\cdot\exp\left(\frac{E_t - E_i}{kT}\right)\right] + \frac{\tau_n}{1+\Gamma_n}\left[p + n_i\exp\left(\frac{E_i - E_t}{kT}\right)\right]}. \tag{11}$$

Γ_n and Γ_p are the enhancement factors that include the effects of electric field assisted tunneling on the emission of electron and hole from a trap respectively. The above parameters unlisted are shown in Table 1.

Where $\Delta E_{n,p}$ is the energy range in which tunneling can occur for an electron or a hole, and u is the variable of integration. K_n and K_p are factors including the reduced tunnel mass m_{t} (m_{t}=0.0135m_0).

Table 1 The expressions of the relevant parameters in the model

Parameters	Expression
C_{Rad}	$\frac{1}{n_i^2}\frac{8\pi}{h^3c^2}\int_0^{\infty}\frac{\varepsilon(E)\alpha(E)E^2\mathrm{d}E}{\exp\left(\frac{E}{kT}\right)-1}$
A_{bbt}	$-\frac{q^2\sqrt{2m_e^*}}{4\pi^3h^2\sqrt{E_g}}$
B_{bbt}	$\frac{n\sqrt{m_e^*/2E_g^{3/2}}}{2q\hbar}$
$\Gamma_{n,p}$	$\frac{\Delta E_{n,p}}{kT}\int_0^1\exp\left(\frac{\Delta E_{n,p}}{kT}u-k_{n,p}u^{3/2}\right)\mathrm{d}u$
$K_{n,p}$	$\frac{4}{3}\frac{\sqrt{2m_t\Delta E_{n,p}^3}}{q\frac{h}{2\pi}\lvert E\rvert}$

4 Applications of LBIC

To date, LBIC as a nondestructive method has been widely used for infrared photodiode array characterization. The big challenge is to quantify the relationship between LBIC mapping and parameters that influence the electrical performance of devices. The main issue of this section is the application with respect to extracting material and device parameters. Lately, a scanning photocurrent map (a two-dimensional LBIC) has been also widely used to study the electrical transport in nano-electronic devices.

4.1 Junction depth and length

The temperature dependence of the peak-to-peak LBIC measurements on p-n junction was first examined by Redfern et al. [25], indicating that a saturation state can be reached under low temperatures. Under the saturation conditions, the junction resistance may be enough to dominate the resistance of each of the possible current paths. Therefore, the peak to peak magnitude of LBIC is independent of the bulk material properties. Other parameters including the junction geometry can be examined by the LBIC peak-to-peak magnitude, greatly reducing the complexity of the analysis. Simulated LBIC peak-to-peak magnitudes as a function of temperature in HgCdTe photodiodes with different components are shown in Figure 4 [30].

The condition of threshold temperature for $\mathrm{Hg_{0.69}Cd_{0.31}Te}$ is below 200 K. The effects of junction depth and length on LBIC profiles in $\mathrm{Hg_{0.69}Cd_{0.31}Te}$ photodiodes at 170 K below the threshold temperature are shown in Figure 5. It has been found that there is a linear relationship between the magnitude of LBIC peak and the size of junction depth and length. For the photodiodes with greater depth, more photo-generated electrons in p-type region can be swept across the junction, which results in a stronger LBIC signal. On the other hand, loop circuit resistance is reduced by shortening of the distance between the contact and junction in the photodiodes with longer length. Therefore, LBIC current also becomes larger when the junction length becomes larger [30].

4.2 Minority carrier diffusion length

The minority carrier diffusion length is a key indicator of material quality and device performance. The dependence of laser beam induced current (LBIC) on minority carrier

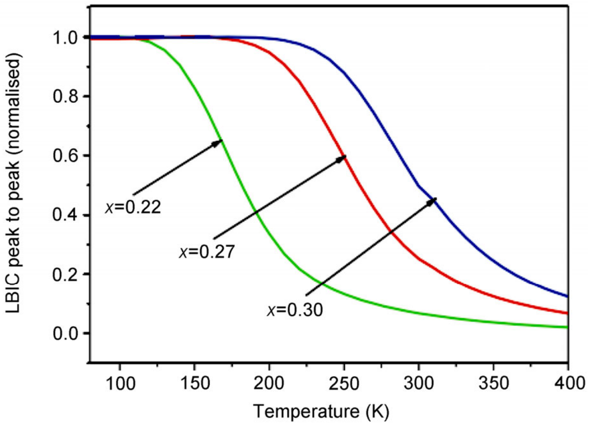

Figure 4 (Color online) Simulated LBIC peak-to-peak magnitudes as a function of temperature in $\mathrm{Hg_{1-x}Cd_xTe}$ photodiodes. Reprinted with permission from ref. [30] © 2013, © Springer.

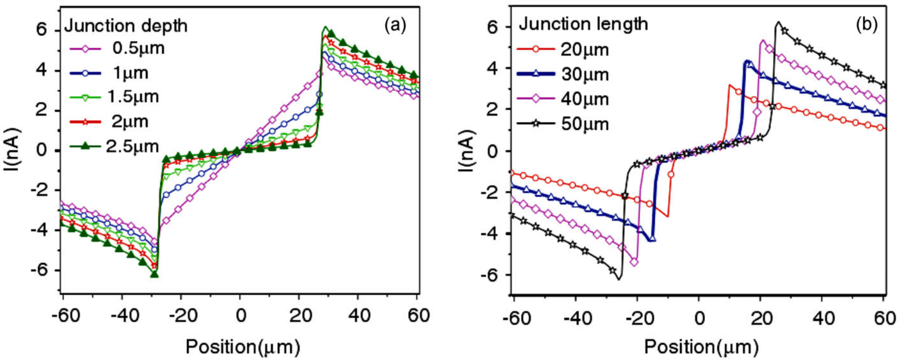

Figure 5 (Color online) (a) LBIC profiles with different depths of $\mathrm{Hg_{0.69}Cd_{0.31}Te}$ p-n junction and (b) LBIC profiles with different lengths of $\mathrm{Hg_{0.69}Cd_{0.31}Te}$ p-n junction. Reprinted with permission from ref. [30] © 2013, © Springer.

diffusion length of n-on-p HgCdTe photodiode has been investigated earlier [11,44]. In the standard diffusion length (L_p) test method, the procedure may bring about damage to the p-n junction. The test structure is also difficult to fabricate because of the need for electrical contact on the p-n junction unit as shown in Figure 6(a). In contrast, the LBIC test structure consists of only two Ohmic contacts at remote positions on either side of the device(s). The decay of the LBIC as the laser spot is scanned away from the edge of p-n junction is related to the diffusion length in p-type region. The characteristic diffusion length (L) can be obtained by fitting a simple exponential function to the LBIC curve. The exponential formula for the attenuation curve in p-type region is given by [45]

$$|I_{\mathrm{LBIC}}(d)| = k\cdot \mathrm{e}^{-\frac{d}{L}}. \tag{12}$$

Here, k is the proportional coefficient; d is the distance from laser spot location to the boundary of p-n junction; and L is the characteristic diffusion length.

In two characteristic ways of diffusion length, the attenuation curves in p-type region are both related to the minority carrier diffusion length. When the laser spot is near the carrier diffusion length from a built-in electric field, the photogenerated electron-hole pairs can diffuse to be separated by the built-in field. The only difference is that the separated carriers recombine via return current paths, i.e, the internal and external closed circuits (two electrodes are both in p region). A LBIC signal can be measured in an external closed circuit of LBIC in this phenomenon. However, the separated carriers are directly collected by the electrodes in p region and n region of the standard protocol. Therefore, there may be a negligible difference between the size of L and L_p. One can extract the ratio coefficient of L/L_p from the experimental results using two different methods.

The standard diffusion length (L_p) and the characteristic diffusion length (L) tested by LBIC in HgCdTe photodiodes with different doping concentrations are shown in Figures 6 and 7, respectively [44].

The diffusion lengths extracted by both these methods are listed in Table 2 [44]. It is found that the L/L_p ratio is close to 1 and is independent of the doping concentration distribution. At the same time, the value of L/L_p ratio remains the same, irrespective of the size of carriers's SRH lifetime and mobility. Therefore, the characteristic diffusion length by LBIC can be considered equivalent with the standard diffusion length.

4.3 Localized junction leakage characterization

The effect of localized defects is one of the main limitations in the performance of HgCdTe infrared focal plane arrays. Such defects, including voids; line dislocations; and triangles, may influence the overall integrity of the p-n junction and significantly degrade the performance of the photodi-

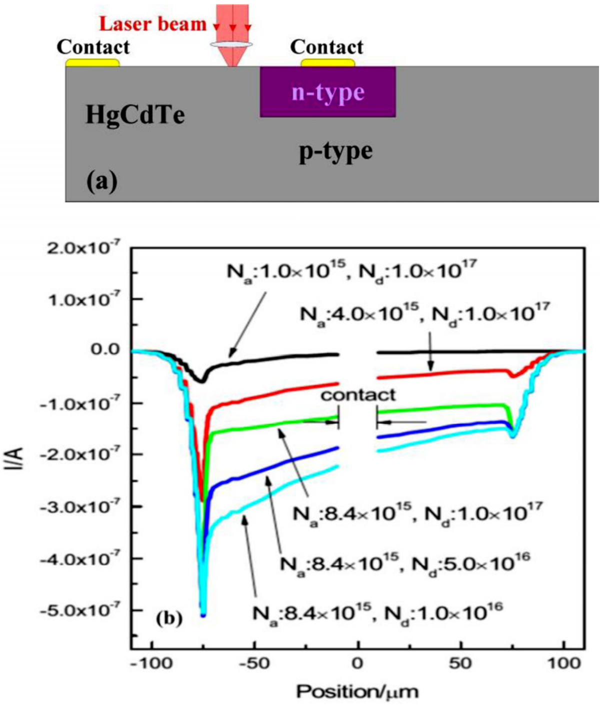

Figure 6 (Color online) (a) The standard diffusion length (L_p) test structure (b) the standard diffusion length (L_p) test in HgCdTe photodiodes with different doping concentrations. Reprinted with permission from ref. [44] © 2009, Chinese Physical Society.

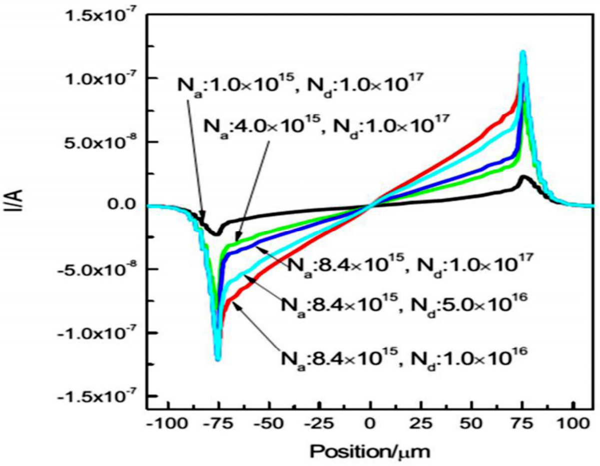

Figure 7 (Color online) The LBIC test for characteristic diffusion length (L) in HgCdTe photodiodes with different doping concentrations. Reprinted with permission from ref. [44] © 2009, Chinese Physical Society.

Table 2 The extracted L/L_p under different doping concentration N_a and N_b. Reprinted with permission from ref. [44] © 2009, Chinese Physical Society

N_a (10^{15} cm^{-3})	N_d (10^{17} cm^{-3})	Characteristic diffusion length L (μm)	Standard diffusion length L_p (μm)	L/L_p
1.0	1.0	8.34	7.81	1.07
4.0	1.0	6.09	5.73	1.06
8.4	1.0	5.34	4.97	1.07
8.4	5.0	5.41	5.02	1.08
8.4	1.0	5.40	5.06	1.07

odes due to the localized junction leakage. LBIC as an efficient and nondestructive tool is used for the localized junction leakage characterization in the photodiodes. Redfern et al. [4,9] studied the LBIC profiles when a small localized leakage region was introduced at various positions along the horizontal portion of the junction. The leakage current was simulated by including a small piece of metal that was Ohmic to both sides of the junction [10]. The model structure of the p-n junction with localized junction leakage path is shown in Figure 8.

It was indicated that when the leakage point is asymmetric inside the device, the asymmetry in the LBIC line profile can be obtained by this leakage model introduced by a small metallic region. However, the assumption by bringing in metal with large conductance in the HgCdTe photodiodes is not very practical.

On the basis of this, Feng et al. [7] improved the leakage model by including a small HgCdTe region with extremely short carrier lifetime instead of the metallic region previously. Many factors, such as trap assisted tunneling, generation-recombination (g-r) and diffusion current, can influence the junction leakage current. Dark current dominant mechanisms change with the operating temperature. The temperature dependence of the LBIC profiles is shown in Figure 9.

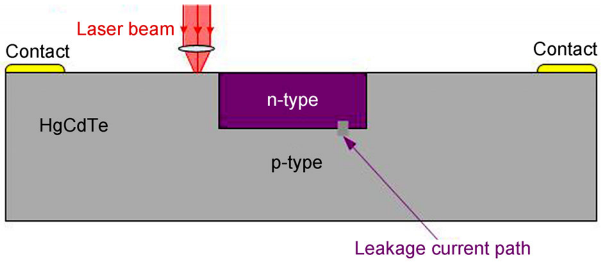

Figure 8 (Color online) The model structure of the p-n junction with localized junction leakage path along the horizontal portion of the junction.

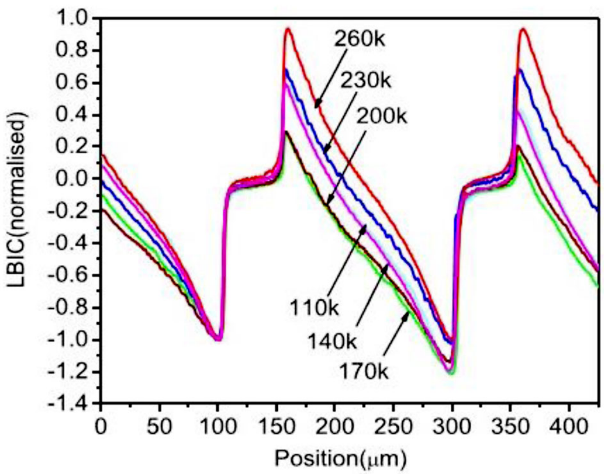

Figure 9 (Color online) The LBIC measurements are taken at a range of temperatures from 110 K to 260 K. Reprinted with permission from ref. [7] © 2013, American Institute of Physics.

The asymmetric LBIC profile can indicate that there is localized leakage somewhere inside the sample structure. The localized defects reduce the resistance of the return current path crossing the junction via the localized leakage, and most current flow through the leakage current path and fail to contribute to the external circuit current. In addition, the temperature dependence of symmetry in the LBIC profile reflects the change in the dominating mechanism of dark current from a certain degree.

It can be observed that the LBIC profiles have different distributions for different temperatures. Below 170 K, the diffusion and generation recombination dark currents are very small. However, with increasing the temperature, the deep level traps are activated that lead to a lower SRH lifetime. The LBIC profile tends to be more asymmetric with increasing temperature. When temperature is above 170 K, the diffusion current component becomes dominant. Then, the leakage current is relatively reduced with the diffusion current being dominant at higher temperatures. The LBIC profile becomes more symmetric with increasing temperature above 170 K. However, when the localized leakage point is situated at the center in the device, it is very difficult to confirm whether there is leakage in the diode because the distribution of LBIC profile is symmetrical. Therefore, in most situations, the asymmetric LBIC profile may indicate that there is localized leakage somewhere inside the sample structure.

4.4 Electrically active defects-related junction transformation

Recent study [6,26,46–49] shows that the phenomenon of extended defects induced by semiconductor manufacturing process always exists in HgCdTe infrared arrays, such as in B^+ ion implantation and pulse laser drilling for the formation of p-n junction. Those defects may be sensitive to temperature and laser excitation intensity, and play a very significant role in the junction transformation. Hu et al. [5,6] first observed that B ion implantation damage induced defects can potentially produce a deformation of the LBIC in As-doped long-wavelength HgCdTe infrared detector pixel arrays. This discovery unveiled an application of LBIC for the corresponding implant-induced defects analysis and characterization. Afterwards, Qiu et al. [26] also found the effects of temperature-dependent localized defects in a new type of femtosecond-laser-drilling-induced HgCdTe photodiodes. Correlated theoretical models for trap-related p-n junction transformation have been proposed to analyze the deformation of LBIC curve induced by the extended defects.

The model structure of the p-n junction transformation in As-doped long-wavelength $Hg_{1-x}Cd_xTe$ ($x \approx 0.224$) infrared arrays under different temperatures is shown in Figure 10. When the temperature is relatively high, the deep levels (acceptor-type) induced by the ion implantation damage are fully activated and can trap significant numbers of free electrons, which are temperature sensitive. It makes the B$^+$ ion implantation region be n$^-$-type or p-type as shown in Figures 10(b)–(c). Furthermore, the laser beam intensity is another key point that determines the reversion. The photo-generated carriers, are comparable to the temperature induced intrinsic carriers, and create an n$^+$-type to n$^-$-type reversion [6]. At cryogenic temperatures the implantation-damage induced traps in the n$^+$ region are almost inactivated, therefore, a typical n$^+$-on-p junction is formed.

In addition, the mixed conduction effect for p-type narrow-bandgap HgCdTe materials must be taken into account, which is mainly caused by the higher electronic mobility compared with that of holes and the temperature-rising-generated by large number of intrinsic carriers; thus the narrower the forbidden bandgap, the more obvious is the mixed conduction effect. The mixed conduction, together with As-doping amphoteric behavior, makes the p-type absorption layer transform to an n-type layer at near room temperature. At moderate temperature, the coupling n-n$^+$-on-p junction is formed. Qiu et al. [26] measured experimentally the Hall coefficient profiles as a function of temperature in p-type Hg-vacancy $Hg_{1-x}Cd_xTe$ ($x\approx 0.27$) samples as shown in Figure 11, where the material will transform to n-type material when temperatures above 200 K.

Ion implantation traps, As-doping amphoteric behavior, and the mixed conduction effect, are the main reasons for inducing the polarity reversion coupling of LBIC at different temperatures. Figure 12 shows the experimental results of the polarity inversion and coupling of LBIC in As-doped long-wavelength HgCdTe infrared detector pixel arrays.

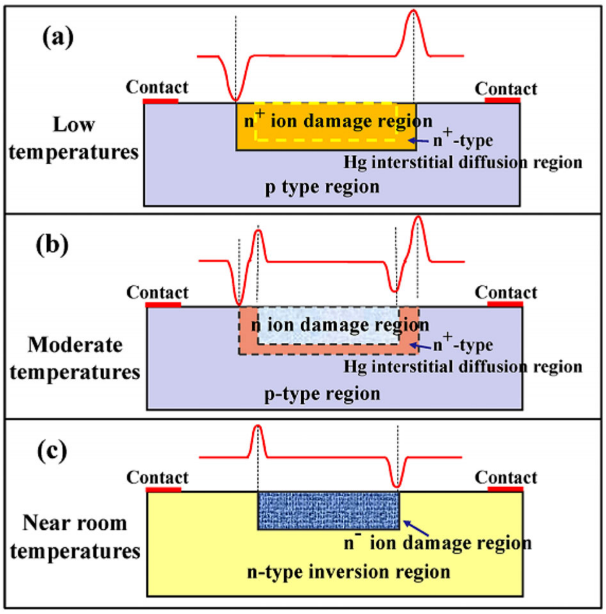

Figure 10 (Color online) Proposed p-n junction transformation models (a) at low temperature where the typical n$^+$-on-p junction is formed, (b) at moderate temperature where the n-n$^+$-on-p junction is formed, and (c) at near room temperature where the n$^-$-on-n junction are formed. Reprinted with permission from ref. [5] © 2012, American Institute of Physics.

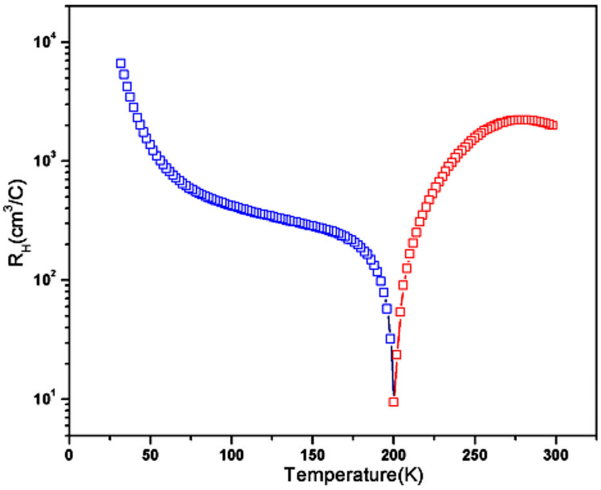

Figure 11 (Color online) Temperature dependency of Hall coefficients. The R_H was positive at temperatures below 200 K (green square symbol), and negative at temperatures above 200 K (red square symbol). Reprinted with permission from ref. [26] © 2014, American Institute of Physics.

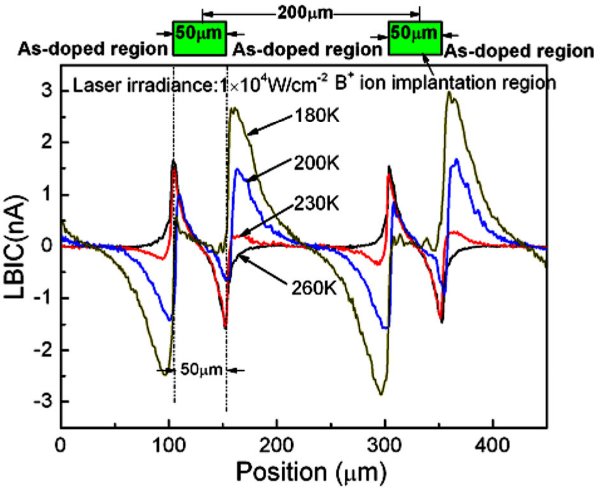

Figure 12 (Color online) Experimental results of temperature-dependent LBIC signal profiles with a laser power density of 1×10^4 W/cm^2. Reprinted with permission from ref. [5] © 2012, American Institute of Physics.

4.5 Scanning photocurrent microscopy characterization for emerging nano-devices with two-dimensional materials

More recently, scanning photocurrent microscopy (SPCM, a typical two-dimensional LBIC mapping) has been widely applied to study electrical properties of a large number of advanced nanostructure devices, such as carbon nanotubes transistors [50–52], graphene transistors [53], MoS_2 transistors [54–58] and semiconductor nanowires [59–64].

LBIC is generated by the separation of photo-generated electrons and holes, a process which is very sensitive to the presence of local built-in electric fields. LBIC is favorable for the study of electrical transport properties of nano-electronic devices. The properties of internal p-n junctions in ambipolar carbon nanotube (CNT) transistors have been investigated by Ahn using the SPCM method [44]. The localized peak photocurrent (PC) spots near both electrode contacts are obviously shown in an SPCM image, which are mainly due to electronic band bending (or equivalently, a local electric field) near the metal/CNT interfaces. The polarity of the PC indicates that the electronic band bends upward towards the middle of the CNT (see the second inset of Figure 13). Moreover, SPCM can also provide important information about Schottky contacts, band structure in nanostructure/metal interfaces, and detection of local defects [52,59].

Due to the extremely high electron mobility, unique mechanical flexibility, and atomic layer thickness, graphene is considered as one of the ideal materials for new optoelectronic devices [65]. However, the quantum efficiency and low absorption cross section of graphene strongly limit its use in high-performance optoelectronic devices [66]. The properties of graphene in devices can be modified by nanoscale antennas through their characteristic surface plasmon [67–69]. A integrated plasmonic antenna-graphene sandwich photodetector was reported by Fang et al. [70] Raman images of different plasmonic antenna structures showed the spatial and spectral regions of strongest antenna-graphene coupling in the device (heptamers structure). The performance of the different regions in the device was characterized by photocurrent measurements along the line scan direction. It was shown that antenna-patterned regions can significantly enhanced the photocurrent compared with the unpatterned regions of the device (see Figure 14(c)). Additionally, the photocurrent can also be controlled by applying a gate bias, achieving active device tuning and switching as shown in Figure 14(d). Miao et al. [71] and Guo et al. [72] report a graphene/InAs nanowire vertically stacked heterojunction infrared photodetector, with a large photoresponsivity and $I_{\text{light}}/I_{\text{dark}}$ ratio. LBIC mapping characterizations show there is a relatively weak photoresponsivity in typical graphene FETs. The strong photocurrent is mainly generated at the metal/graphene interfaces (Points A and C) which is attributed to the separation of photogenerated electron-hole pairs by built-in electric fields, as shown in Figure 15. However, the photocurrent at point B is very weak because of the absence of a strong built-in field in the bulk graphene. Therefore, most photogenerated electron-hole pairs would recombine before flowing into the Source/Drain electrodes, seldom contributing to the photocurrent. A new heterojunction could form at the interface between the InAs nanowire and graphene because of the different work functions and band energies, enhancing photoresponsivity.

Lee et al. [73] used scanning photocurrent microscopy (SPCM) to explore the impact of electrical contacts and sheet edges on charge transport through graphene devices under different operational conditions. The phenomenon of n-type to p-type transition in devices was observed by photocurrent images under different gate voltages (see Figure 16).

In addition, single-layer MoS_2 applied to optoelectronic devices is widely studied because of its large intrinsic bandgap (1.8 eV), and in-plane mobility apart from other remarkable mechanical properties [74–76]. Buscema et al. [77] studied the photoresponse of single-layer MoS_2 field effect transistors (FET) by scanning photocurrent microscopy. It Figure 17 shows that photocurrent generation in single-layer MoS_2 is dominated by the photothermoelectric effect and not by the separation of photogenerated electron-hole pairs across the Schottky barriers at the MoS_2/electrode interfaces.

5 Summary

Accompanied by the technological development and exten-

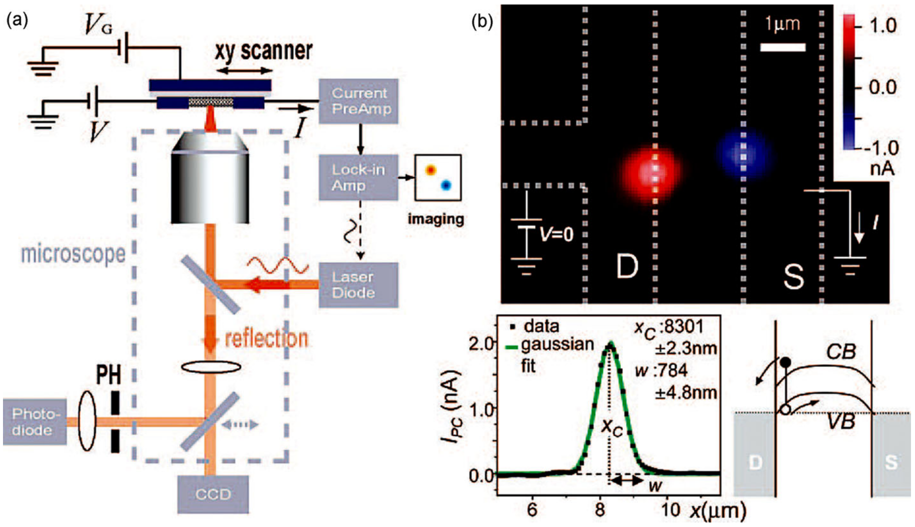

Figure 13 (Color online) (a) Schematic diagram of the SPCM setup. (b) SPCM image of a semiconducting CNT device D1. Left inset: Gaussian fit of one PC spot for determining the peak position and width. Right inset: physical mechanism of the contact PC generation. Reprinted with permission from ref. [50] © 2007, American Chemical Society.

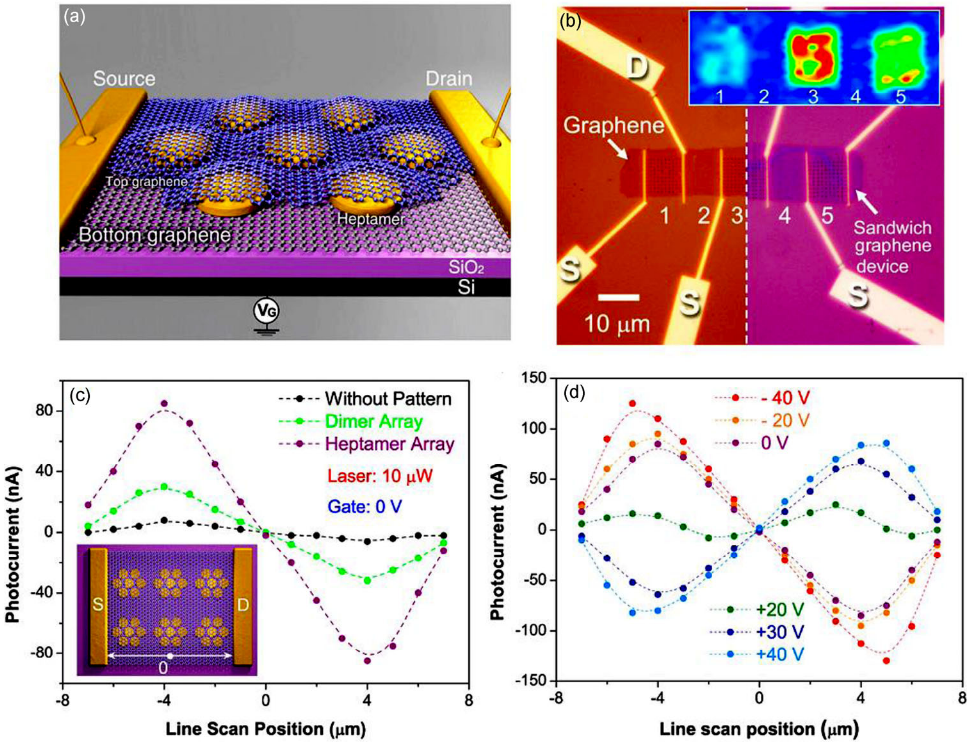

Figure 14 (Color online) Photocurrent characterization of antenna-graphene sandwich devices. (a) Schematic illustration of a single gold heptamer sandwiched between two monolayer graphene sheets. V_G is the gate voltage. (b) Raman mapping of the as-fabricated device before (left) and after (right) deposition of the second graphene layer. (c) Photocurrent measurements show anti-symmetric photocurrent responses from the different regions of the device corresponding to specific plasmonic antenna geometries, obtained along the line scan direction. (d) Measured photocurrent for gate bias V_G between −40 to +40 V for the heptamer antenna-patterned region 3 of the device. Reprinted with permission from ref. [70] © 2012, American Chemical Society.

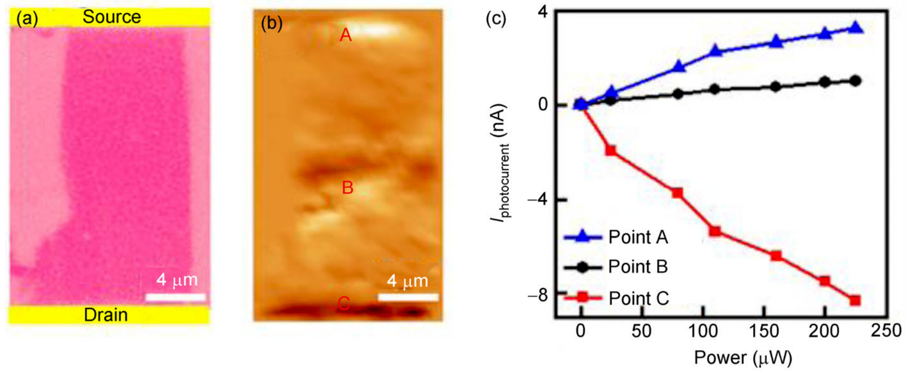

Figure 15 (Color online) (a) Optical image of a back-gated typical graphene field effect transistor. (b) LBIC mapping at room temperature with the laser wavelength of λ = 532 nm. (c) I_{photo} as a function of the incident power taken at point A, B, and C with a laser wavelength of 1 μm. Reprinted with permission from ref. [71] © 2014, Wiley-VCH.

sive applications of infrared focal plane arrays, position-dependent LBIC or PC mapping has triggered a wave of research interest for device characterization at the early stage of the fabrication process. LBIC or PC mapping technologies rely on the scanning laser system that is close to the diffraction limit, making them highly sensitive to spatially resolved electric fields and localized nonuniformities in infrared materials. The spatially resolved information about electrical properties makes the extraction of performance parameters in infrared materials easier and more efficient through the establishment of accurate simulation models. Furthermore, the resulting photoelectric information serves as an important guideline for understanding the electron band structure, carrier transport processes, and optoelectronic mechanisms in emerging nano-devices with two-dimensional materials. The high flexibility, low operational costs, and excellent spatial resolution properties of LBIC enable this method to be a highly useful tool for the

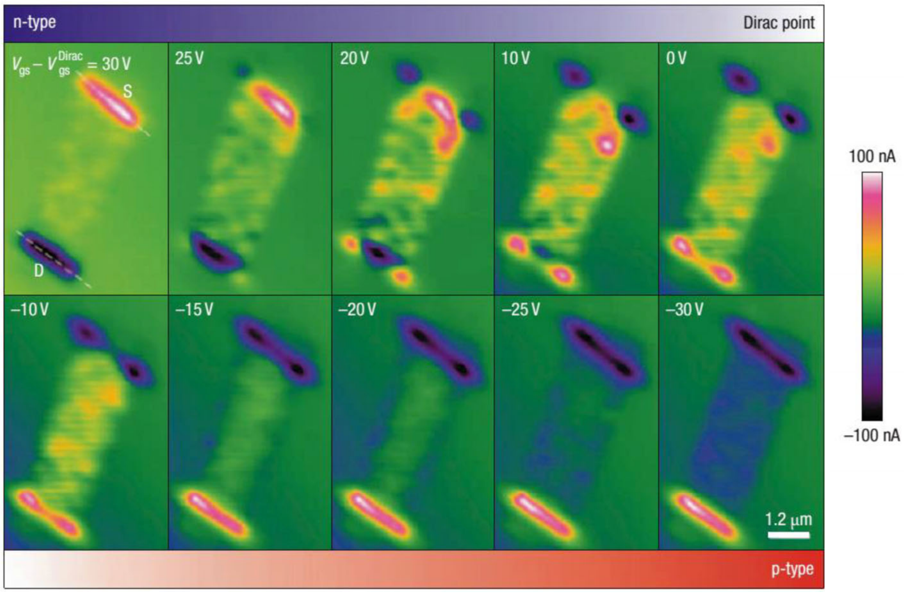

Figure 16 (Color online) Spatially resolved photocurrent maps at various transport regimes of a graphene device. The sequence of images displaying the n- to p-type transition, as the gate voltage is swept from 30 to −30 V. The dashed lines in the top left image indicate the position of the drain (D) and source (S) electrodes. Reprinted with permission from ref. [73] © 2008, Nature Publishing Group.

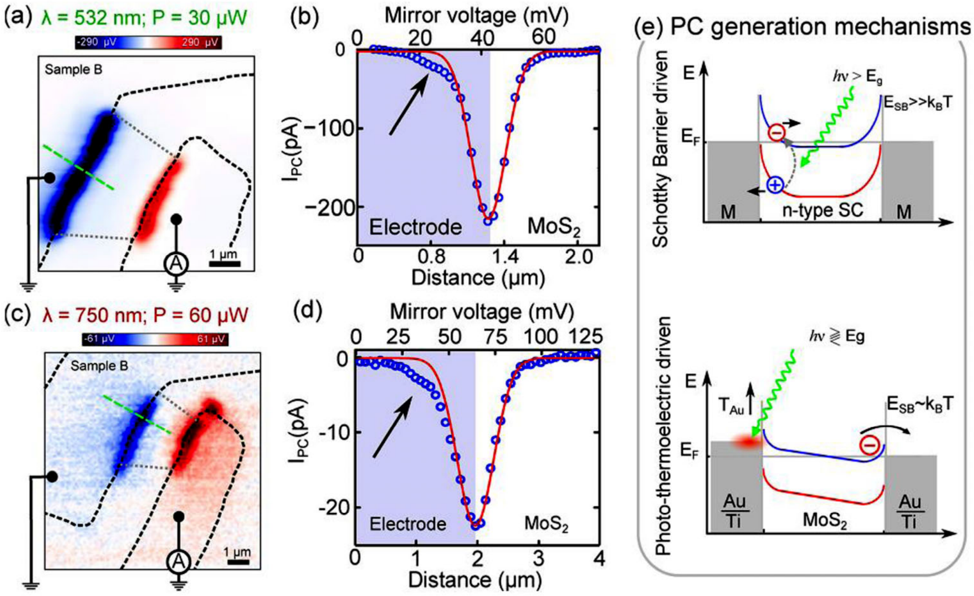

Figure 17 (Color online) Photovoltage map of a single layer MoS_2 FET using an excitation wavelength of 532 nm (a) and 750 nm (c). (b), (d) Photocurrent profile across the line cut in panels a, b (open blue circles). The solid red line is a Gaussian fit of the data and the arrow points at the photocurrent tail generated when the laser spot is scanned over the electrode. (e) Schematic of the photoresponse mechanism in a device dominated by photothermoelectric effect. The conduction band is drawn in blue while the valence band is drawn in red. Reprinted with permission from ref. [77] © 2013, American Chemical Society.

characterization and optimization of future optoelectronicand photovoltaic studies.

The authors thank James Torley from the University of Colorado at Colorado Springs for critical reading of the manuscript. This work was supported by the State Key Program for Basic Research of China (Grant No. 2014CB921600), the National Natural Science Foundation of China (Grant Nos. 11322441 and 11274331), and the Fund of Shanghai Science and Technology Foundation (Grant No. 14JC1406400).

1 Wallmark J T. A new semiconductor photocell using lateral photoeffect. Proc IRE, 1956, 45: 474–483
2 Bajaj J, Bubulac L O, Newman P R, et al. Spatial mapping of electrically active defects in HgCdTe using laser beam induced current. J Vac Sci Technol A, 1987, 5: 3186–3187
3 Musca C A, Redfern D A, Dell J M, et al. Laser beam induced current as a tool for HgCdTe photodiode characterization. Microelectron J, 2000, 31: 537–544
4 Redfern D A, Smith E, Musca C A, et al. Interpretation of current flow in photodiode structures using laser beam-induced current for

characterization and diagnostics. IEEE Trans Electron Dev, 2006, 53: 23–31

5 Hu W D, Chen X S, Ye Z H, et al. Polarity inversion and coupling of laser beam induced current in As-doped long-wavelength HgCdTe infrared detector pixel arrays: Experiment and simulation. Appl Phys Lett, 2012, 101: 181108

6 Hu W D, Chen X S, Ye Z H, et al. Dependence of ion-implant-induced LBIC novel characteristic on excitation intensity for long-wavelength HgCdTe-based photovoltaic infrared detector pixel arrays. IEEE J Sel Top Quant, 2013, 19: 4100107

7 Feng A L, Li G, He G, et al. The role of localized junction leakage in the temperature-dependent laser-beam-induced current spectra for HgCdTe infrared focal plane array photodiodes. J Appl Phys, 2013, 114: 173107

8 Redfern D A, Musca C A, Dell J M, et al. Correlation of laser-beam-induced current with current-voltage measurements in HgCdTe photodiodes. J Electron Mater, 2004, 33: 560–571

9 Redfern D A, Musca C A, Dell J M, et al. Characterization of electrically active defects in photovoltaic detector arrays using laser beam-induced current. IEEE Trans Electron Dev, 2005, 52: 2163–2174

10 Yin F, Hu W D, Zhang B, et al. Simulation of laser beam induced current for HgCdTe photodiodes with leakage current. Opt Quantum Electron, 2009, 41: 805–810

11 Redfern D A, Thomas J A, Musca C A, et al. Diffusion length measurements in p-HgCdTe using laser beam induced current. J Electron Mater, 2001, 30: 696–703

12 Musca C A, Redfern D A, Smith E, et al. Junction depth measurement in HgCdTe using laser beam induced current (LBIC). J Electron Mater, 1999, 28: 603–610

13 Gluszak E A, Hinckley S, Kamran E. Determination of junction depth and related current phenomena using laser-beam-induced current. Proc SPIE, 2004, 5274: 331–341

14 Hu W D, Chen X S, Yin F, et al. Analysis of temperature dependence of dark current mechanisms for long-wavelength HgCdTe photovoltaic infrared detectors. J Appl Phys, 2009, 105: 104502

15 Hu W D, Chen X S, Ye Z H, et al. Accurate simulation of temperature dependence of dark current in HgCdTe infrared detector assisted by analytical modeling. J Electron Mater, 2010, 39: 981–985

16 Zha F X, Zhou S M, Ma H L, et al. Laser drilling induced electrical type inversion in vacancy-doped p-type HgCdTe. Appl Phys Lett, 2008, 93: 151113

17 Zha F X, Li M S, Shao J, et al. Femtosecond laser-drilling-induced HgCdTe photodiodes. Opt Lett, 2010, 35: 971–973

18 Zhou S M, Zha F X, Guo Q T, et al. The morphology of micro hole pn junction in p-type HgCdTe formed by femtosecond laser drilling. J Infrared Millim Waves, 2010, 29: 337–341

19 Martyniuk M, Sewell R H, Westerhout R, et al. Electrical type conversion of p-type HgCdTe induced by nanoimprinting. Appl Phys, 2011, 109: 096102

20 Gluszak E A, Hinckley S. Contactless junction contrast of HgCdTe n-on-p-type structures obtained by reactive ion etching induced p-to-n conversion. J Electron Mater, 2001, 30: 768–773

21 Fang W, Ito K, Redfern D A. Parameter identification for semiconductor diodes by LBIC imaging. SIAM J Appl Math, 2002, 62: 2149–2174

22 Hong X K, Lu H, Zhang D B. Study on the structure characteristics of HgCdTe photodiodes using laser beam-induced current. Opt Quantum Electron, 2013, 45: 623–628

23 Bajaj J, Tennant W E, Newman P R. Laser beam induced current imaging of surface nonuniformity at the HgCdTe/ZnS interface. J Vac Sci Technol A, Vac Surf Films, 1988, 6: 2757–2759

24 Bajaj J, Tennant W E, Zucca R, et al. Spatially resolved characterization of HgCdTe materials and devices by scanning laser microscopy. Semicond Sci Technol, 1993, 8: 872–887

25 Redfern D A, Fang W, Ito K, et al. Low temperature saturation of p-n junction laser beam induced current signals. Solid-State Electron, 2004, 48: 409–414

26 Qiu W C, Cheng X A, Wang R, et al. Novel signal inversion of laser beam induced current for femtosecond-laser-drilling induced junction on vacancy-doped p-type HgCdTe. J Appl Phys, 2014, 115: 204506

27 Busenberg S, Fang W, Ito K. Modeling and analysis of laser beam induced current images in semiconductors. SIAM J Appl Math, 1993, 53: 187–204

28 Qiu W C, Hu W D, Lin T, et al. Temperature-sensitive junction transformations for mid-wavelength HgCdTe photovoltaic infrared detector arrays by laser beam induced current microscope. Appl Phys Lett, 2014, in press

29 Hu W D, Ye Z H, Liao L, et al. A 128×128 long-wavelength/mid-wavelength two-color HgCdTe infrared focal plane array detector with ultra-low spectral crosstalk. Opt Lett, 2014, 39: 5130–5133

30 Feng A L, Li G, He G, et al. Dependence of laser beam induced current on geometrical sizes of the junction for HgCdTe photodiodes. Opt Quantum Electron, 2014, 46: 1277–1282

31 Baugher B, Churchill H, Yang Y F, et al. Optoelectronic devices based on electrically tunable p-n diodes in a monolayer dichalcogenide. Nat Nanotech, 2014, 9: 262–267

32 Balasubramanian K, Burghard M, Kern K, et al. Photocurrent imaging of charge transport barriers in carbon nanotube devices. Nano Lett, 2005, 5: 507–510

33 Zhang Y P, Deng W, Zhang X J, et al. *In situ* integration of squaraine-nanowire-array-based schottky-type photodetectors with enhanced switching performance. ACS Appl Mater Interfaces, 2013, 5: 12288–12294

34 Buscema M, Groenendijk D J, Steele G A, et al. Photovoltaic effect in few-layer black phosphorus PN junctions defined by local electrostatic gating. Nature Commun, 2014, 5: 4651

35 Yu Y Q, Jie J S, Jiang P, et al. High-gain visible-blind UV photodetectors based on chlorine-doped n-type ZnS nanoribbons with tunable optoelectronic properties. J Mater Chem, 2011, 21: 12632–12638

36 Wang J L, Zou X M, Xiao X H, et al. Floating gate memory based monolayer MoS_2 transistor with metal nanocrystals embedded in gate dielectrics. Small, 2014, doi: 10.1002/smll.201401872

37 Hu W D, Chen X S, Yin F, et al. Simulation and design consideration of photoresponse for HgCdTe infrared photodiodes. Opt Quantum Electron, 2008, 40: 1255–1260

38 Guo N, Hu W D, Chen X S, et al. Optimization for mid-wavelength InSb infrared focal plane arrays under front-side illumination. Opt Quantum Electron, 2013, 45: 673–679

39 Hu W D, Chen X S, Ye Z H, et al. An improvement on short wavelength photoresponse for a heterostructure HgCdTe two-color infrared detector. Semicond Sci Technol, 2010, 25: 045028

40 Wenus J, Rutkowski J, Rogalski A. 2D analysis of double layer heterojunction HgCdTe photodiodes. IEEE Trans Electron Devices, 2001, 48: 1326–1332

41 Orsogna D D, Tobin S, Bellotti E. Numerical analysis of a very long-wavelength HgCdTe pixel array for infrared detection. J Electron Mater, 2008, 37: 1349–1355

42 Keasler C A, Moresco M, Orsogna D D, et al. 3D numerical analysis of As-diffused HgCdTe planar pixel arrays. Proc SPIE, 2010, 7780: 77800J

43 Ji X L, Liu B Q, Xu Y, et al. Deep-level traps induced dark currents in extended wavelength $In_xGa_{1-x}As$/InP photodetector. J Appl Phys, 2013, 114: 224502

44 Yin F, Hu W D, Quan Z J, et al. Determination of electron diffusion length in HgCdTe photodiodes using laser beam induced current. Acta Phys Sin, 2009, 58: 7885–7889

45 Ong V, Wu D. Determination of diffusion length from within a confined region with the use of EBIC. IEEE Trans Electron Dev, 2001, 48: 332–337

46 Bubulac L O, Tennant W E. Role of Hg in junction formation in ion-implanted HgCdTe. Appl Phys Lett, 1987, 51: 355–357

47 Bubulac L O. Dependence of junction formation on substrate in implanted HgCdTe. Appl Phys Lett, 1985, 46: 976–978

48 Arias J M, Zandian M, Bajaj J, et al. Molecular beam epitaxy HgCdTe growth-induced void defects and their effect on infrared photodiodes. J Electron Mater, 1995, 24: 521–524

49 Buell A A, Pham L T, Newton M D, et al. Physical structure of molecularbeam epitaxy growth defects in HgCdTe and their impact on

two-color detector performance. J Electron Mater, 2004, 33: 662–666

50 Ahn Y H, Tsen A W, Kim B, et al. Photocurrent Imaging of p-n Junctions in Ambipolar Carbon Nanotube Transistors. Nano Lett, 2007, 7: 3320–3323

51 Balasubramanian K, Fan Y W, Burghard M, et al. Photoelectronic transport imaging of individual semiconducting carbon nanotubes. Appl Phys Lett, 2004, 84: 2400–2402

52 Freitag M, Tsang J C, Bol A, et al. Imaging of the schottky barriers and charge depletion in carbon nanotube transistors. Nano Lett, 2007, 7: 2037–2042

53 Xia F N, Mueller T, Golizadeh-mojarad R, et al. Photocurrent imaging and efficient photon detection in a graphene transistor. Nano Lett, 2009, 9: 1039–1044

54 Wu C C, Jariwala D, Sangwan V K, et al. Elucidating the photoresponse of ultrathin MoS_2 field-effect transistors by scanning photocurrent microscopy. J Phys Chem Lett, 2013, 4: 2508–2513

55 Oriol L S, Dominik L, Metin K, et al. Ultrasensitive photodetectors based on monolayer MoS_2. Nat Nanotech, 2013, 8: 497–501

56 Britnell L, Ribeiro R M, Eckmann A, et al. Strong light-matter interactions in heterostructures of atomically thin films. Science, 2013, 340: 1311–1314

57 Song X F, Hu J L, Zeng H B. Two-dimensional semiconductors: Recent progress and future perspectives. J Mater Chem C, 2013, 1: 2952–2969

58 Zeng H B, Zhi C Y, Zhang Z H, et al. “White” graphene: Boron nitride nanoribbons via boron nitride nanotube unwrapping. Nano Lett, 2010, 10: 5049–5055

59 Ahn Y, Dunning J, Park J. Scanning photocurrent imaging and electronic band studies in silicon nanowire field effect transistors. Nano Lett, 2005, 5: 1367–1370

60 Gu Y, Kwak E, Lensch J, et al. Near-field scanning photocurrent microscopy of a nanowire photodetector. Appl Phys Lett, 2005, 87: 043111

61 Miao J S, Hu W D, Guo N, et al. Single InAs nanowire room-temperature near-infrared photodetectors. ACS Nano, 2014, 8: 3628–3635

62 Dufaux T, Boettcher J, Burghard M, et al. Photocurrent distribution in graphene-CdS nanowire devices. Small, 2010, 6: 1868–1872

63 Howell S L, Padalkar S, Yoon K, et al. Spatial mapping of efficiency of GaN/InGaN nanowire array solar cells using scanning photocurrent microscopy. Nano Lett, 2013, 13: 5123–5128

64 Allen J E, Hemesath E R, Lauhon L J. Scanning photocurrent microscopy analysis of Si nanowire field-effect transistors fabricated by surface etching of the channel. Nano Lett, 2009, 9: 1903–1908

65 Luo L B, Chen J J, Wang M Z, et al. Near-Infrared light photovoltaic detector based on GaAs nanocone array/monolayer graphene schottky junction. Adv Funct Mater, 2014, 24: 2794–2800

66 Bonaccorso F, Sun Z, Hasan T, et al. Graphene photonics and optoelectronics. Nat Photon, 2010, 4: 611–622

67 Echtermeyer T J, Britnell L, Jasnos P K, et al. Strong plasmonic enhancement of photovoltage in grapheme. Nat Commun, 2011, 2: 458

68 Liu Y, Cheng R, Liao L, et al. Plasmon resonance enhanced multicolour photodetection by grapheme. Nat Commun, 2011, 2: 579

69 Luo L B, Zeng L H, Xie C, et al. Light trapping and surface plasmon enhanced high-performance NIR photodetector. Sci Rep, 2014, 4: 3914–3918

70 Fang Z Y, Liu Z, Wang Y M, et al. Graphene-antenna sandwich photodetector. Nano Lett, 2012, 12: 3808–3813

71 Miao J S, Hu W D, Guo N, et al. High-responsivity graphene/InAs nanowire heterojunction near-infrared photodetectors with distinct photocurrent on/off ratio. Small, 2014, in press, doi: 10.1002/smll.201402312

72 Guo N, Hu W D, Liao L, et al. Anomalous and highly-efficient InAs nanowire phototransistors based on majority carrier transport at room temperature. Adv Mater, 2014, in press, doi: 10.1002/adma.201403664

73 Lee E J, Balasubramanian K, Weitz R T, et al. Contact and edge effects in grapheme devices. Nat Nanotech, 2008, 3: 486–490

74 Yin Z Y, Li H, Jiang L, et al. Single-layer MoS_2 phototransistors. ACS Nano, 2012, 6: 74–80

75 Lee H S, Min S W, Chang Y G, et al. MoS_2 nanosheet phototransistors with thickness-modulated optical energy gap. Nano Lett, 2012, 12: 3695–3700

76 Choi W, Cho M Y, Konar A, et al. High-detectivity multilayer MoS_2 phototransistors with spectral response from ultraviolet to infrared. Adv Mater, 2012, 24: 5832–5836

77 Buscema M, Barkelid M, Zwiller V, et al. Large and tunable photothermoelectric effect in single-layer MoS_2. Nano Lett, 2013, 13: 358–363